Noncontact rotation, levitation, and acceleration of flowing liquid metal wires

Yahua He[a], Jianbo Tang[b], Kourosh Kalantar-Zadeh[b], Michael D. Dickey[c,1], and Xiaolin Wang[a,d,1]

[a]Institute for Superconducting and Electronic Materials, Australian Institute for Innovative Materials, University of Wollongong, Wollongong, NSW 2500, Australia; [b]School of Chemical Engineering, University of New South Wales, Sydney, NSW 2052, Australia; [c]Department of Chemical and Biomolecular Engineering, North Carolina State University, Raleigh, NC 27695; and [d]Australian Research Council Center of Excellence in Future Low Energy Electronics Technologies, University of Wollongong, Wollongong, NSW 2500, Australia

Edited by David Weitz, Department of Physics, Division of Engineering and Applied Science, Harvard University, Cambridge, MA; received September 23, 2021; accepted December 20, 2021

This paper reports the noncontact manipulation of free-falling cylindrical streams of liquid metals into unique shapes, such as levitated loops and squares. Such cylindrical streams form in aqueous media by electrochemically lowering the interfacial tension. The electrochemical reactions require an electrical current that flows through the streams, making them susceptible to the Lorentz force. Consequently, varying the position and shape of a magnetic field relative to the stream controls these forces. Moreover, the movement of the metal stream relative to the magnetic field induces significant forces arising from Lenz's law that cause the manipulated streams to levitate in unique shapes. The ability to control streams of liquid metals in a noncontact manner will enable strategies for shaping electronically conductive fluids for advanced manufacturing and dynamic electronic structures.

liquid metal wire | noncontact manipulation | levitated patterns | electromagnetism

Noncontact methods of manufacturing and manipulation can minimize disrupting objects of interest. Objects can be manipulated in a noncontact manner by magnetic methods (levitation and tweezers) (1, 2), acoustic manipulation (3, 4), optical tweezers (5), and other techniques (6, 7). However, to date, free-flowing liquid streams have been particularly difficult to manipulate in a noncontact manner. Realizing highly controlled changes in directionality or complex shaping of liquids, especially without disrupting the cross-sectional shape of the stream, is a challenge. Here, we explore the noncontact manipulation of free-flowing streams of liquid metals (LMs). Gallium-based LMs (Galinstan, the eutectic alloy of gallium indium and tin used in this work) have recently received significant attention due to their promises of soft and stretchable metallic conductors, low melting points, and simultaneous fluidity and metallic properties at room temperature as well as low toxicity (8–15).

LM alloys are seemingly unlikely candidates to form stable fluid streams due to their enormous surface tension and water-like viscosity, which favor the formation of droplets (Fig. 1*A*). However, electrochemical oxidation of the surface of the LM in basic solution lowers the effective tension of the LM to extremely low values (16, 17). This electrochemical manipulation of interfacial tension enables various fascinating phenomena, such as reversible deformation (18), patterning (19), heartbeat effects (20), "superfluid-like" penetration through porous media (21), and other electrochemical effects (22–29). Most importantly, the presence of oxide species on the LM also enables long, stable wire-like streams of metal to form as it exits a nozzle into the solution (17, 30) (Fig. 1*B*). Because of their cylindrical cross-section and metallic conductivity, we call these fluidic streams liquid metal wires (LMWs), which form narrow diameters (~100 to 200 μm). Although normally LM is not responsive to magnetic fields, the current passing through the wire to drive the electrochemical reactions makes it susceptible to magnetic forces via the Lorentz force (Fig. 1*C*). The Lorentz force arises by applying a magnetic field normal to the direction of electrical current. The Lorentz force is normal to both the current and magnetic field, as described by the so-called "left-hand rule."

In this work, we control the displacement of free-falling LMWs at room temperature using the Lorentz force. Because LM is soft, it provides almost no resistance to manipulation via the Lorentz force and therefore, accelerates radially. The displacement of the LMWs relative to the magnet also induces a secondary force according to Lenz's law (i.e., a drag force that opposes the motion at the periphery of the magnet). Thus, the combination effects of the Lorentz force and Lenz's law drive the metal into shapes that mirror the circumference of the magnet while levitating the metal. As shown here, the behavior depends on the location of the magnet relative to the LMW. We demonstrate and characterize the unique ability to manipulate LM streams in a noncontact manner using only a relatively low applied voltage and a common magnet.

Results

The LM was aspirated into a syringe (diameter of 0.26 mm) and pumped at a volumetric flow rate (VFR) controlled by a syringe pump. Electrodes attached to the syringe needle applied 1.5 V to the metal relative to a negative electrode. We chose this potential

Significance

Streams of fluids, particulates, and other flowing media are difficult to control after they have left a nozzle. Here, we present the noncontact manipulation of a free-flowing stream of liquid metal. Such streams form by electrochemically lowering the interfacial tension. The electrochemical reactions make the streams into soft current–carrying conductors presenting minimal resistance to manipulation via the Lorentz force in the magnetic field. Meanwhile, the movement of the stream induces a secondary force arising from Lenz's law that causes the manipulated streams to levitate in unique shapes. This work, which exploits these forces in a visually stunning manner, enables shaping of fluids in a noncontact manner.

Author contributions: X.W. conceived the study; Y.H. and X.W. designed and performed experiments; Y.H., M.D.D., and X.W. analyzed data and conducted discussion and analysis of the mechanism; Y.H., M.D.D., and X.W. wrote the paper; J.T. worked on the figures; J.T. and K.K.-Z. contributed to discussion and revision of the manuscript; and Y.H., J.T., K.K.-Z., M.D.D., and X.W. participated in the preparation of the manuscript.

The authors declare no competing interest.

This article is a PNAS Direct Submission.

This open access article is distributed under Creative Commons Attribution-NonCommercial-NoDerivatives License 4.0 (CC BY-NC-ND).

[1]To whom correspondence may be addressed. Email: mddickey@ncsu.edu or xiaolin@uow.edu.au.

This article contains supporting information online at http://www.pnas.org/lookup/suppl/doi:10.1073/pnas.2117535119/-/DCSupplemental.

Published February 1, 2022.

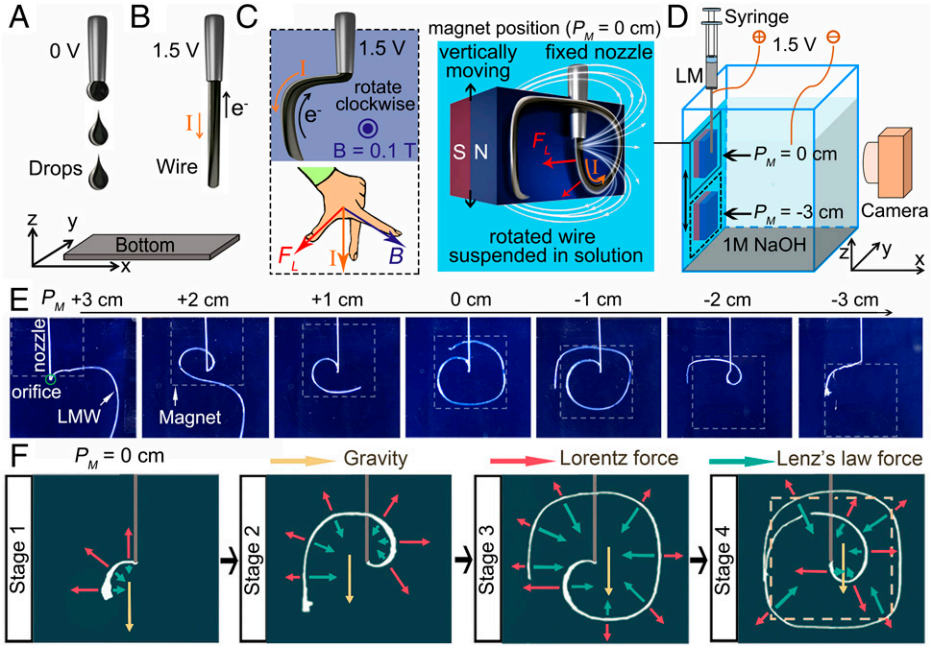

Fig. 1. Shaping free-flowing liquid metal wires by the Lorentz force and Lenz's law: (*A*) drops form at 0 V and (*B*) a liquid metal wire at 1.5 V. (*C*) Current-carrying LMW rotated by the Lorentz force within a magnetic field in which N and S refer to the north and south poles of the magnet. (*D*) Schematic illustration of the experimental setup; a blue piece of paper covered one wall of the vessel to facilitate imaging. (*E*) Photographs showing the LMW path resulting from different positions of the magnet with the N pole outward. The dotted lines indicate the location and the shape of the magnet. (*F*) False-colored images of LM (white) showing four sequences of frames with a force diagram and motion analysis. The yellow dotted line denotes the periphery of the magnet.

because it results in the formation of wires as the LM exits the syringe needle (17). The experiments proceeded in a 1-mol/L NaOH solution inside a plastic vessel (Fig. 1*D*). The syringe remained immersed in the solution close to the vessel wall to be in proximity to an external magnet placed flush against the exterior wall.

We defined the vertical position of the magnet (P_M) relative to the fixed position of the needle orifice. That is, when $P_M = 0$, the center of the magnet is at the same vertical height as the orifice. To vary the Lorentz force, we moved the magnet by P_M from +3 to −3 cm (positive values indicate that the magnet is in an elevated position relative to the orifice). The north (N) pole of the magnet (0.1 T) faced the needle of the syringe unless otherwise stated.

Fig. 1*E* shows the results of the LMWs' motion at a flow rate of 2 μL/s when the P_M was changed from +3 to −3 cm with an interval of 1 cm. When the magnet is centered with the needle outlet (P_M = 0), the LMW experiences uniform magnetic field lines at the nozzle exit. Consequently, it moves in a circular pattern driven by the Lorentz force (Movie S1). However, for high P_M (+3 and +2 cm) or low P_M (−2 or −3 cm), the LMW experiences "fringe" (i.e., diverging) field lines from the off-centered magnet. Consequently, the LMWs move in a spiral shape. The circular motion of the LMWs occurred for the P_M between +1 and −1 cm, while the spiral motions occurred for other positions.

A force analysis helps to explain these trajectories. The LMW should be subjected to three primary forces: gravity (G), the Lorentz force (F_L), and Lenz's law force (F_{Lenz}). G accelerates the LMW downward. F_{Lenz} is the drag force induced by changes in the magnetic flux as the metal wire moves away from (or toward) the magnet. The Lorentz force, defined by the formula $\boldsymbol{F_L} = \boldsymbol{B} \cdot \boldsymbol{I} \cdot \boldsymbol{L}$ (B is magnetic field intensity, I is current, and L is the length of LMW in the magnetic field), causes the LMW to deviate from its straight, downward path as it exits the nozzle. The viscous drag only dissipates energy and does not dictate the path of the LMW (*SI Appendix*, section D). We neglect the pressure from electrostatic ($P_E = {\varepsilon_r \varepsilon_0 U^2}/{D^2} = 6 \times 10^{-7}$ Pa; ε_0 is the vacuum permittivity, ε_r is the relative permittivity of the 1 M NaOH solution, U is the external potential, and D is the distance between electrodes) and Laplace pressure ($\Delta P = {\gamma}/{R} = 2 \times 10^{-4}$ Pa; γ is the interfacial tension, and R is the radius of the LMW) since they are negligible compared with the pressure from the Lorentz force ($P_L = {\boldsymbol{B} \cdot i_m}/{\pi R} = 38$ Pa; i_m is the measured current through LMW) (*SI Appendix*, section E).

Fig. 1*F* shows four typical sequences of frames (four stages) of the temporal evolution of the spiral when P_M = 0. At stage 1 (S1), the Lorentz force directs LMW outward in a clockwise pattern. Lenz's force is negligible at this initial stage since the LM is still within the uniform field of the magnet. At stage 2 (S2), the LMW moves near the left edge of the magnet. At this location, changes in magnetic flux are greatest, and thus, the LMW experiences maximum Lenz's force and a decreased Lorentz force (since it is no longer in the strongest part of the magnetic field). Thus, its outward motion slows at this location. Yet, fresh LMW continues to pump from the nozzle and emerges under the control of the relatively large Lorentz force. Thus, it moves outward radially but in a direction influenced by the instantaneous shape of the metal. For example (stage 2), the metal that emerges from the nozzle directs to the right (the "3 o'clock position"). In stage 3 (S3), the LMW nearly wraps around the edge of the magnet. Finally, in stage 4 (S4), the LMW fully covers the circumference of the magnet and roughly adopts its square shape. These four stages repeat to create multiple loops of metal around the magnet perimeter. Taken in sum, the LMW experiences the Lorentz force as it exits the nozzle, while Lenz's law force slows the motion and stops the wire at the circumference of the magnet.

Given the importance of the Lorentz force and Lenz's law, we sought to explore their impact on the LMW behavior. The Lorentz force is determined by the product of the magnetic field strength (B), current, and the length (L) of LMW. Lenz's law effect is determined by the rate of change in magnetic flux

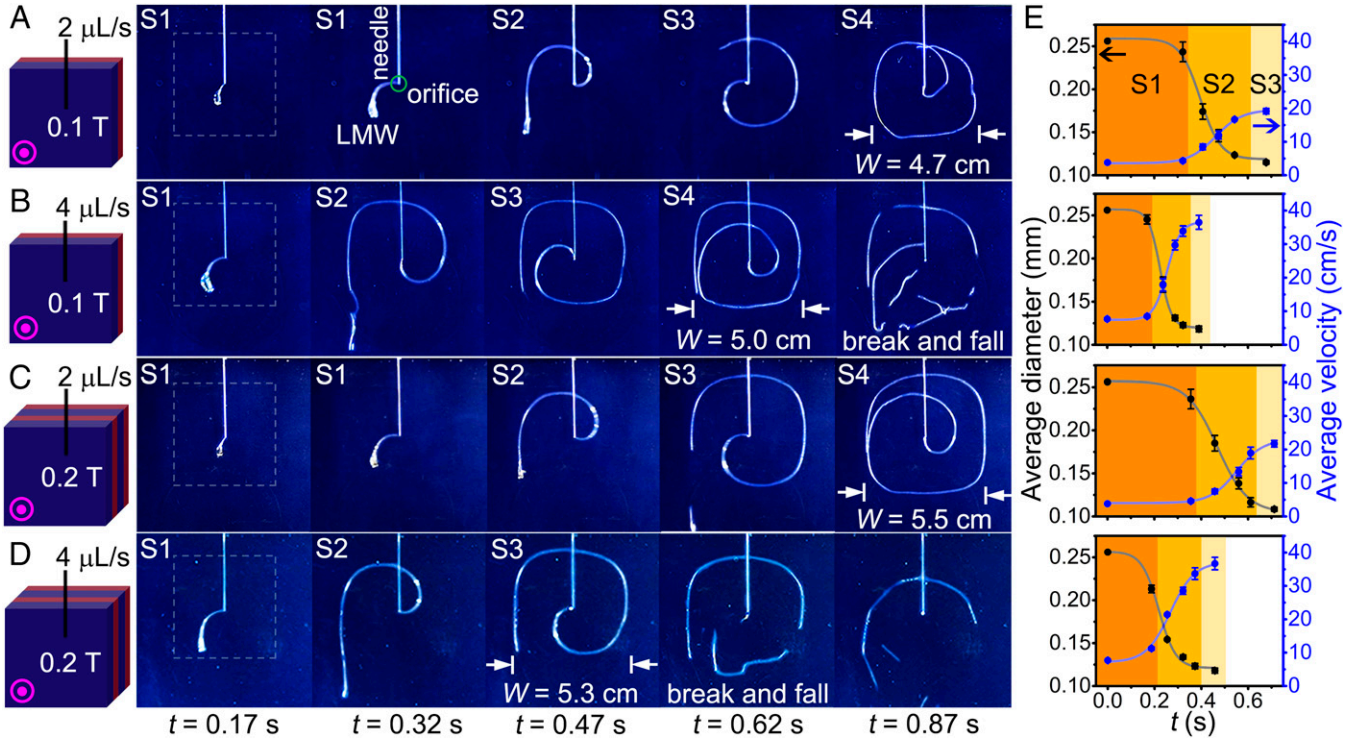

Fig. 2. Sequence of photographs recording the motion of a LMW under different experimental conditions with the magnet center fixed at $P_M = 0$ cm (N pole outward): (*A*) 2 μL/s, 0.1 T; (*B*) 4 μL/s, 0.1 T; (*C*) 2 μL/s, 0.2 T; and (*D*) 4 μL/s, 0.2 T. The square-shaped magnet has dimensions of 5 × 5 × 0.5 cm^3. (*E*) The changes of velocity and diameter of LMW at the three stages S1, S2, and S3.

$(\partial\phi_B/\partial t \sim \boldsymbol{B}\cdot\boldsymbol{v})$, where v is the velocity ($v = L/t$) of the LMW. The length of the LMW depends on the VFR in a fixed time ($\boldsymbol{L} \sim VFR$). Thus, we varied the B and VFR to study both effects of the Lorentz force and Lenz's law. The results are shown in Fig. 2, in which $P_M = 0$ in all cases.

Fig. 2*A* shows the trajectory for VFR = 2 μL/s and B = 0.1 T. The trajectory is a "semicircle swing arm" moving clockwise like that depicted in Fig. 1. The same path occurs for the south (S) pole pointing outward, except that the LMW moves counterclockwise.

Increasing VFR to 4 μL/s while keeping B = 0.1 T (Fig. 2*B*) increases the length of the LMW for the same time duration for all the stages (the columns in Fig. 2). Stated differently, the increased flow rate decreases the amount of time to reach each stage. For example, the LMW reached stage 4 after 0.62 s, whereas it takes 0.87 s when the flow rate is half as much (2 μL/s). The increased Lorentz force drives the faster motion at high VFRs due to the longer wires that form. We observe similar behavior by doubling the flow rate at higher magnetic fields (0.2 T; by simply stacking one more magnet) (Fig. 2 *C* and *D*). A more detailed statistical analysis for elapsed time and the size of the trajectory, including height (H_{max}) and width (W_{max}), is shown in *SI Appendix*, Fig. S1.

To a first approximation, the behavior of the LMW at 0.2 T is similar to that at 0.1 T at the same flow rate (e.g., compare Fig. 2 *A* and *C*). This is expected considering that the effect of Lorentz (radial acceleration) and Lenz (radial deceleration) both depend linearly on B. This similarity is apparent by comparing the velocities and diameters (d) of the LMW as shown in Fig. 2*E*. The fourth stage is excluded in the plot since the effect of Lenz's law causes the LMW to fully stop at the edge of the magnet. For VFR = 2 μL/s, the velocity can reach about 20 cm/s in 0.7 s, while for VFR = 4 μL/s, the velocity reaches up to 35 cm/s in as short as 0.45 s. The acceleration causes a concurrent decrease in wire diameter (black data in Fig. 2*E*) as expected. According to Newton's second law $\frac{\partial p}{\partial d} = -\rho\frac{\partial v}{\partial t}$, where ρ is the density and p is the pressure of LMW, a decrease in diameter leads to an increase of velocity. An increase of velocity further decreases the diameter of the wire, causing further acceleration in a positive feedback loop (*SI Appendix*, section D). The decrease in wire diameter corresponds with wire elongation, which can further increase the Lorentz force.

In the experiments reported in Fig. 2, the metal immediately experiences the Lorentz force as it exits the nozzle since $P_M = 0$. We explored moving the magnet farther below the nozzle so that the LMW would experience Lenz's law as it reached the edge of the magnet (Fig. 3). The strength of the Lenz's law effect depends on the magnetic field and velocity of the LMW.

To vary velocity, we first pumped the metal at a VFR of 2 μL/s without a magnet to investigate the velocity of the LMW as a function of distance from the nozzle (Fig. 3 *A*, *Inset*). The LMW emerges initially from the nozzle as a small bead. Gravity pulls this bead from the nozzle, and a cylindrical stream follows. This acceleration causes the leading bead to reach a maximum value of ~25 cm/s at the position of −6 cm. Beyond this position, the velocity of the LMW reaches a steady state. The velocity change can be fit with an exponential function.

Based on this understanding of the velocity profile of the LMW, we moved magnets to different positions to explore the role of velocity on the behavior of the LMW. The positions are marked as B, C, D, and E in Fig. 3*A*, corresponding to the positions of −4, −5, −6, and −9 cm, respectively. The images of the LMWs' trajectories for different P_M are shown in Fig. 3 *B*–*E*. For the P_M = −4 cm, the metal wire undergoes a clockwise spiral motion within a small region near the upper left edge of the magnet. The trajectory becomes larger for P_M = −5 cm. There is a conspicuous difference in the trajectory for P_M = −6 cm. The trajectory remarkably adopts the same square shape of the magnet circumference (Movie S2). The case is the same for P_M = −9 cm. This is because the velocities at P_M = −6 and −9 cm are enough for inducing sufficient Lenz's law effect to

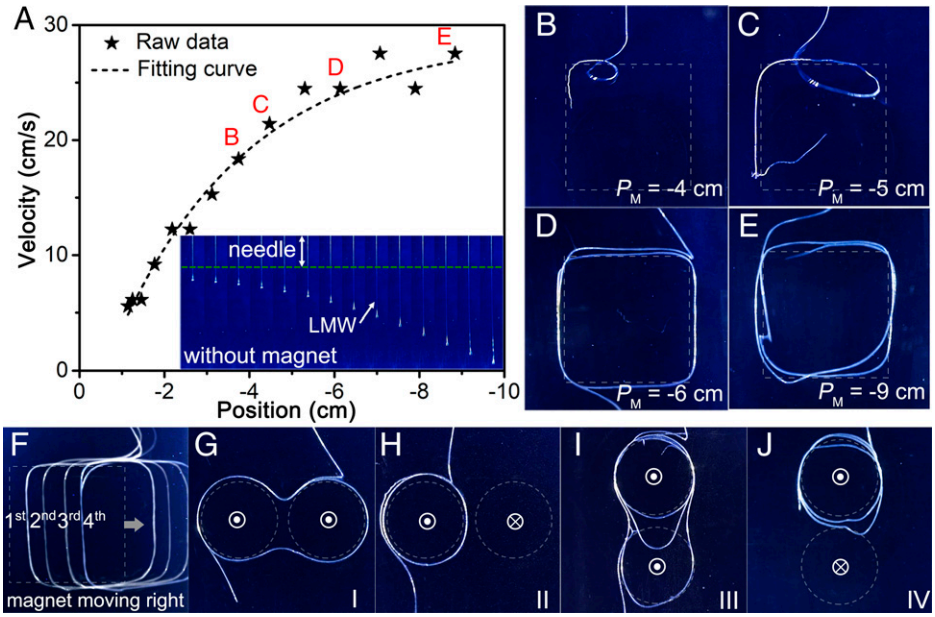

Fig. 3. (*A*) The velocity of LM pumped from the needle at 2 μL/s without a magnet, with *A*, *Inset* showing snapshots of the trajectories. The green dotted line represents the needle outlet. (*B*–*E*) The typical trajectories under the 0.1 T magnetic field at different magnet positions with the N pole outward. (*F*) Dynamic patterns by moving the magnet horizontally. Complex magnetic field arrangements using two circular magnets with diameters of 3.5 cm and (*G* and *H*) N/S poles placed side by side and (*I* and *J*) N/S poles arranged vertically with a distance of 0.5 cm. The dotted lines indicate the location and the shape of the magnet.

confine the LM at the periphery of the magnet. The combination of the Lorentz force and the Lenz's law effect causes the LMW to wrap clockwise.

To illustrate the diversity of shapes that are possible with this effect, we performed experiments with different magnet configurations at $P_M = -6$ cm (*SI Appendix*, Fig. S2). The role of the magnet is apparent by moving the magnet horizontally (Fig. 3*F* and Movie S3) with different speeds (*SI Appendix*, Fig. S3), which shows that the patterning can be dynamic and highly dependent on magnet position. Moreover, some complex shapes are realized by using two magnets, which are arranged in various configurations, such as the shape of the number 8 in configuration I (Fig. 3*G* and Movie S4) and configuration III (Fig. 3*I* and Movie S6). Moreover, the LMW circles around one magnet only by just reversing the north/south (N/S) pole, as in configuration II (Fig. 3*H* and Movie S5) and configuration IV (Fig. 3*J* and Movie S7; *SI Appendix*, Fig. S4 has more details). The levitation of the LMW around the magnet perimeter is driven by the Lenz's law effect. In addition, the stability of the patterned structures in time is discussed in *SI Appendix*, section D (*SI Appendix*, Fig. S5).

The electrical current, which arises from electrochemical surface oxidation, plays an important role in the Lorentz force. However, the Lenz's law effect can suppress the current in the LMW. To illustrate this effect, we measured the electrical current that passes through the LMWs under different conditions: case 1, absence of LMW and magnet; case 2, free-falling LMW without a magnet; and case 3, free-falling LMW with a magnet (located at different positions) (*SI Appendix*, section C).

For case 1, the current is ∼0.4 mA, with the external voltage fixed at 1.5 V. For case 2, the current increases by ∼200 times to ∼80 mA as the LMW forms (*SI Appendix*, Fig. S6). The large current of LMW originates from the oxidizing surface reaction. The current increases linearly with the length of the LMW due to an increase in surface area with length (*SI Appendix*, Fig. S7). For case 3, the measured currents show periodic oscillation associated with the wires wrapping around the perimeter and ultimately, falling. This happens with different frequencies and magnitudes depending on the magnet positions (Fig. 4). The frequency data are obtained through an fast Fourier transform (FFT) of the current vs. time.

Interestingly, the measured currents in the presence of the magnet are smaller than expected relative to a free-falling wire. The differences between the estimated current (i_e) and measured current (i_m) are significant (Fig. 4 *C*, *F*, and *I*). Faraday's law of induction is applied to quantitatively explain the effect of Lenz's law. For an LMW rotating in a magnet, a potential (U) is induced; $U = \oint (E + v \times B) dl$, and E is electric field along LMW. The $\oint Edl$ term on the right side of the equation shows the contribution of the Lenz's law effect, while $\oint v \times Bdl$ is the Lorentz force on charges by the motion of LMW. When the magnet is placed at positions $P_M = 0$, -6, and -9 cm, the calculated values of $\oint Edl$ are -0.18, -0.81, and -1.63 V, respectively. In comparison, the calculated values of the Lorentz force–induced potential ($\oint v \times Bdl$) for the three magnet positions are only as small as 0.00625, 0.01, and 0.014 V (*SI Appendix*, section E). Thus, the Lenz's law effect should be primarily responsible for the significant current drop.

In this paper, using only 1.5 V and a common magnet, we demonstrated the unique ability to steer free-flowing LMWs in a noncontact manner into paths and suspended shapes. This enables fascinating effects, including rotational motion, levitation, and acceleration. The Lenz's law effect stabilizes the LMW pattern by controlling the current through LMW within a stable range and levitates LMW patterns, while the Lorenz force rotates and accelerates the LMW. Moreover, the transiently stable structures formed here could provide routes to build on this patterning method to stabilize the structures (discussion is in *SI Appendix*, section D) by coextruding a shell (e.g., polymeric material), cooling the receiving substrate (for solidification) (30), or curing the structures in a monomer solution (e.g., hydrogel). The findings help visualize such forces due to the use of soft (and highly conductive) liquid conductors. Thus, this work enables the patterning of useful metallic shapes and offers a strategy for shaping fluids in a noncontact manner.

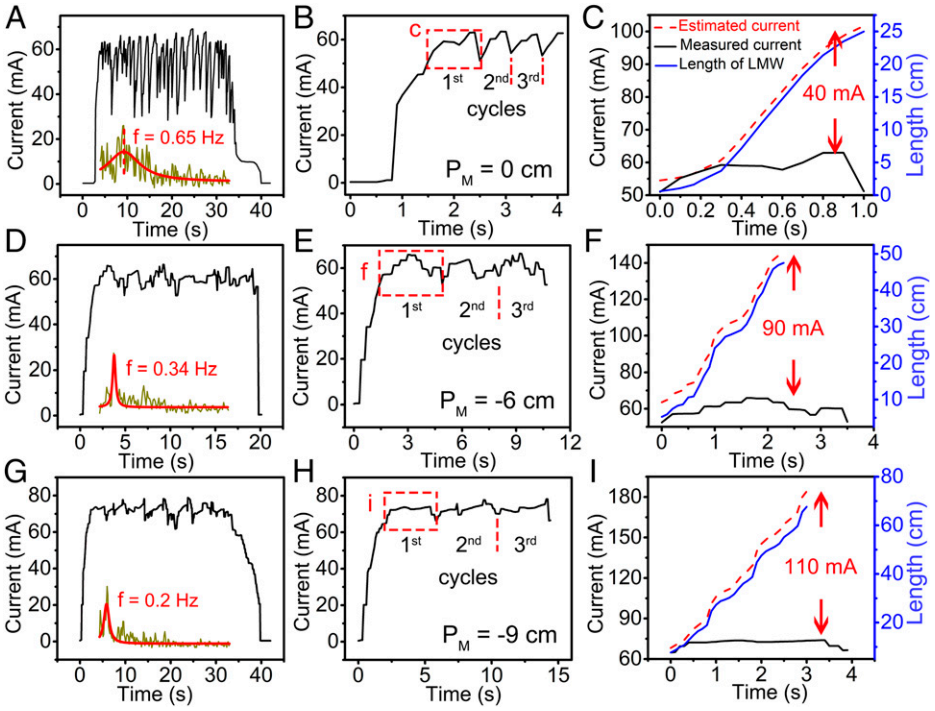

Fig. 4. Current vs. time of LMWs with a magnet placed at different positions. (*A*–*C*) $P_M = 0$ cm, (*D*–*F*) $P_M = -6$ cm, and (*G*–*I*) $P_M = -9$ cm. The current value is synchronized with the periodic formation/disintegration of LMW. *A*, *Inset*, *D*, *Inset*, and *G*, *Inset* are the frequency data through FFT of current. *B*, *E*, and *H* are the first three cycles, and *C*, *F*, and *I* show the current drop in the first cycle induced by the Lenz's law effect. The external voltage is fixed at 1.5 V for all cases.

Materials and Methods

Experiment Setup. A syringe pump injected Galinstan into an electrolyte bath through a needle with a diameter of 0.26 mm at a controlled VFR (2 and 4 μL/s were chosen in this work). Electrodes attached to the syringe needle applied 1.5 V to the metal relative to a negative electrode. The distance between electrodes was 5 cm. All experiments proceeded in a 1-mol/L NaOH solution inside a plastic vessel with dimensions of 15 × 15 × 20 cm^3. The syringe remained immersed in the solution close to the vessel wall to be in proximity to an external magnet placed flush against the exterior wall. The position of the needle remained fixed. We defined the vertical position (P_M) of the magnet relative to the fixed position of the needle orifice. That is, when $P_M = 0$, the center of the magnet is at the same vertical height as the orifice. To vary the Lorentz force and the Lenz's law effect, we moved the magnet by P_M from +3 to −9 cm (positive values indicate that the magnet is in an elevated position relative to the orifice). A camera placed in front of the vessel recorded the motion of the LM.

Velocity. The initial pump-out velocity of the LM was calculated by the equation $v = \frac{VFR}{A}$, where *VFR* is the volumetric flow rate controlled by the syringe pump and *A* is the cross-section area of the needle. Additionally, when the formed liquid wire stream moved in the magnet, the velocity was calculated by the length of the LMW divided by time $v = \frac{L}{t}$, where *L* is the length and *t* is the time.

Electrical Current. All measured electrical current flowing though the LMW was collected by Keithley DMM 2002 on a Labview platform. For free-falling LMW, the current increased with the length of the LMW: $I = 53.4 + 1.933L$, where *I* is the current and *L* is the length of the LMW. When a magnet was presented, the estimated current (Fig. 4) was calculated by the equation.

Data Availability. All data are included in the manuscript and/or supporting information.

ACKNOWLEDGMENTS. X.W. is grateful for support from Australian Research Council (ARC) Future Fellowship Project Grant FT130100778, ARC Laureate Fellowship Grant FL180100053 (K.K.-Z.), and the ARC Center of Excellence in Future Low Electronic Technologies Grant CE170100039. M.D.D. is grateful for support from the NSF CBET-1510772. We thank Mary Tuman and Luke Cunningham for their contribution to the figures.

1. F. C. Moon, *Superconducting Levitation: Applications to Bearings and Magnetic Transportation* (John Wiley & Sons, 2008).
2. X. Wang *et al.*, Intracellular manipulation and measurement with multipole magnetic tweezers. *Sci. Robot.* **4**, eaav6180 (2019).
3. Z. Tian *et al.*, Wave number-spiral acoustic tweezers for dynamic and reconfigurable manipulation of particles and cells. *Sci. Adv.* **5**, eaau6062 (2019).
4. D. Ahmed *et al.*, Rotational manipulation of single cells and organisms using acoustic waves. *Nat. Commun.* **7**, 11085 (2016).
5. A. Ashkin, J. M. Dziedzic, J. E. Bjorkholm, S. Chu, Observation of a single-beam gradient force optical trap for dielectric particles. *Opt. Lett.* **11**, 288–290 (1986).
6. E. H. Brandt, Levitation in physics. *Science* **243**, 349–355 (1989).
7. J. Zhang, Z. Wang, Z. Wang, T. Zhang, L. Wei, In-fibre particle manipulation and device assembly via laser induced thermocapillary convection. *Nat. Commun.* **10**, 5206 (2019).
8. M. D. Dickey, Stretchable and soft electronics using liquid metals. *Adv. Mater.* **29**, 1606425 (2017).
9. T. Daeneke *et al.*, Liquid metals: Fundamentals and applications in chemistry. *Chem. Soc. Rev.* **47**, 4073–4111 (2018).
10. M. D. Bartlett *et al.*, Stretchable, high-k dielectric elastomers through liquid-metal inclusions. *Adv. Mater.* **28**, 3726–3731 (2016).
11. M. R. Khan, C. Trlica, M. D. Dickey, Recapillarity: Electrochemically controlled capillary withdrawal of a liquid metal alloy from microchannels. *Adv. Funct. Mater.* **25**, 671–678 (2015).
12. C. Ladd, J. H. So, J. Muth, M. D. Dickey, 3D printing of free standing liquid metal microstructures. *Adv. Mater.* **25**, 5081–5085 (2013).
13. Q. Wang, Y. Yu, J. Yang, J. Liu, Fast fabrication of flexible functional circuits based on liquid metal dual-trans printing. *Adv. Mater.* **27**, 7109–7116 (2015).
14. T. Liu, P. Sen, C. J. Kim, Characterization of nontoxic liquid-metal alloy galinstan for applications in microdevices. *J. Microelectromech. Syst.* **21**, 443–450 (2011).
15. X. Wang *et al.*, Soft and moldable Mg-doped liquid metal for conformable skin tumor photothermal therapy. *Adv. Healthc. Mater.* **7**, e1800318 (2018).
16. M. R. Khan, C. B. Eaker, E. F. Bowden, M. D. Dickey, Giant and switchable surface activity of liquid metal via surface oxidation. *Proc. Natl. Acad. Sci. U.S.A.* **111**, 14047–14051 (2014).
17. M. Song *et al.*, Overcoming Rayleigh-Plateau instabilities: Stabilizing and destabilizing liquid-metal streams via electrochemical oxidation. *Proc. Natl. Acad. Sci. U.S.A.* **117**, 19026–19032 (2020).
18. Z. Yu, Y. Chen, F. F. Yun, X. Wang, Simultaneous fast deformation and solidification in supercooled liquid gallium at room temperature. *Adv. Eng. Mater.* **19**, 1700190 (2017).

19. Z. Yu, F. F. Yun, X. Wang, A novel liquid metal patterning technique: Voltage induced noncontact electrochemical lithography at room temperature. *Mater. Horiz.* **5**, 36–40 (2018).
20. Z. Yu *et al.*, Discovery of a voltage-stimulated heartbeat effect in droplets of liquid gallium. *Phys. Rev. Lett.* **121**, 024302 (2018).
21. F. F. Yun *et al.*, Voltage-induced penetration effect in liquid metals at room temperature. *Natl. Sci. Rev.* **7**, 366–372 (2020).
22. A. Zavabeti *et al.*, A liquid metal reaction environment for the room-temperature synthesis of atomically thin metal oxides. *Science* **358**, 332–335 (2017).
23. J. Zhang, Y. Yao, L. Sheng, J. Liu, Self-fueled biomimetic liquid metal mollusk. *Adv. Mater.* **27**, 2648–2655 (2015).
24. J. Zhang, R. Guo, J. Liu, Self-propelled liquid metal motors steered by a magnetic or electrical field for drug delivery. *J. Mater. Chem. B Mater. Biol. Med.* **4**, 5349–5357 (2016).
25. S. Y. Tang *et al.*, Liquid-metal microdroplets formed dynamically with electrical control of size and rate. *Adv. Mater.* **28**, 604–609 (2016).
26. J. Tang, X. Zhao, J. Li, Y. Zhou, J. Liu, Liquid metal phagocytosis: Intermetallic wetting induced particle internalization. *Adv. Sci. (Weinh.)* **4**, 1700024 (2017).
27. C. B. Eaker, D. C. Hight, J. D. O'Regan, M. D. Dickey, K. E. Daniels, Oxidation-mediated fingering in liquid metals. *Phys. Rev. Lett.* **119**, 174502 (2017).
28. R. S. Datta *et al.*, Flexible two-dimensional indium tin oxide fabricated using a liquid metal printing technique. *Nat. Electron.* **3**, 51–58 (2020).
29. M. Mayyas *et al.*, Liquid-metal-templated synthesis of 2D graphitic materials at room temperature. *Adv. Mater.* **32**, e2001997 (2020).
30. J. Han *et al.*, Exploring electrochemical extrusion of wires from liquid metals. *ACS Appl. Mater. Interfaces* **12**, 31010–31020 (2020).